ATMOSPHERIC ENVIRONMENT: X 31 (2026) 100479

Contents lists available at ScienceDirect

Atmospheric Environment: X

journal homepage: www.journals.elsevier.com/atmospheric-environment-x

Comparative validation of ENVI-met versions 5.6 and 5.9 against high-resolution in-situ air temperature measurements

Tim Sinsel *, Peer Schöneberger, Helge Simon, Michael Bruse

Department of Geography, Johannes Gutenberg University Mainz, Mainz, 55099, Germany

ARTICLE INFO

Keywords:
Model validation
Urban microclimate
Surface-to-air heat transfer
Air temperature

ABSTRACT

Microclimate simulations are critical for assessing urban heat mitigation strategies, yet they face ongoing challenges regarding computational cost and physical parameterization. This study evaluates the performance of the three-dimensional microclimate model ENVI-met, comparing air temperature prediction of the legacy Version 5.6 against the updated Version 5.9. The updated kernel introduces a revised formulation for surface-to-air sensible heat exchange alongside code optimizations. The validation utilizes a high-resolution air temperature dataset collected around a standalone office building in Aalborg, Denmark, covering a 7-day period with varying meteorological conditions. Detailed statistical analysis, including daytime and nighttime stratification, reveals that both model versions reproduce diurnal temperature cycles with a coefficient of determination (R^2) exceeding 0.94. The updated Version 5.9 demonstrated a reduction in the aggregated Root Mean Square Error (RMSE) from 0.89 K to 0.78 K and successfully reduced systemic Mean Bias Error (MBE) across the domain, with the most distinct improvements observed in the immediate boundary layer of sun-exposed façades. Additionally, the simulation runtime for the observed period decreased by a factor of approximately three. These findings indicate that the algorithmic updates improve physical consistency in resolving near-surface temperature gradients while significantly lowering the computational resources required for microclimate modeling.

1. Introduction

The mitigation of urban heat stress requires predictive tools capable of quantifying the impact of design interventions, ranging from single-tree planting to district-level restructuring (Hatvani-Kovacs et al., 2018; O'Malley et al., 2015; Wong et al., 2021). Current microclimate modeling tools are generally characterized by a trade-off between computational efficiency and physical complexity (Dey and Joshi, 2022; Lam et al., 2021). On one end, radiation-based models such as UMEP, SOLWEIG, RayMan, or SLUCM provide rapid assessments of mean radiant temperature or building surface temperatures (Lieber et al., 2025; Lindberg et al., 2008, 2018; Matzarakis et al., 2010; Wallenberg et al., 2026). While computationally efficient and accessible for iterative design, these tools often lack the aerodynamic and thermodynamic depth required to simulate complex fluid dynamics and accurate air temperature variations within the canopy layer (Jänicke et al., 2021; Liu et al., 2020).

Conversely, high-fidelity LES models, such as PALM-4U, offer superior physical resolution but typically rely on high-performance computing infrastructure (Anders and Maronga, 2025; Maronga et al., 2019). Such hardware dependencies can limit their applicability in standard architectural and urban planning workflows, while representing strong scientific tools. ENVI-met represents a tool occupying the critical middle ground as a holistic, three-dimensional RANS model (Jänicke et al., 2021). Unlike radiation-focused tools, it solves fundamental equations for fluid flow and thermodynamics, linking atmospheric processes with soil hydrology, vegetation physiology, and building physics to represent the urban energy balance (Bruse and Fleer, 1998; Huttner, 2012; Simon, 2016). The most important parameters for determining outdoor thermal comfort were validated by a multitude of studies already (Elraouf et al., 2022; Liu et al., 2021; Tsoka et al., 2018).

However, some of the studies also stated model limitations. First, the model is computationally demanding, with simulation runtimes that can be prohibitive for rapid prototyping (Aleksandrowicz et al., 2023). Second, literature frequently discusses the accuracy of the model by comparing simulations and in-situ measurements, often related to Mean Radiant Temperature (MRT) (Aleksandrowicz et al., 2023; Schöneberger et al., 2025; Sinsel et al., 2022), partly regarding the amplitude of

* Corresponding author.
E-mail address: t.sinsel@geo.uni-mainz.de (T. Sinsel).

https://doi.org/10.1016/j.aeaoa.2026.100479
Received 5 June 2026; Accepted 12 June 2026
Available online 13 June 2026

diurnal temperature cycles or surface-to-air heat transfer (Barnstorf et al., 2023; Detommaso et al., 2021; Eingrüber et al., 2023; Liu et al., 2024). While some of these discrepancies stem from input inaccuracies – specifically the use of generic boundary conditions that fail to capture local advection or solar radiation conditions (Schöneberger et al., 2025) – systematic deviations of sensible heat flux modeling in previous versions indicated a need for internal refinement of the model physics.

In response to these challenges, recent updates to the ENVI-met core (Version 5.9) have addressed both computational speed and physical accuracy. A critical update involves the correction of the resistive heat exchange formulation between surfaces and the first atmospheric layer. The new algorithm replaces a geometric simplification with a physically consistent calculation that distinguishes between the temperature gradient distance and the volumetric heat budget height in near-surface heating rate calculations (Section 2.1). Additionally, the simulation code was optimized aiming to reduce the substantial computational cost associated with detailed CFD simulations. This study evaluates the impact of these updates by comparing the legacy kernel (Version 5.6 – V56) and the updated kernel (Version 5.9 – V59) against a high-resolution validation dataset. The dataset, collected around a stand-alone office building in Aalborg, Denmark, is well-suited for this purpose as it includes air temperature measurements at varying distances from the façade (0.1 m to 2.0 m) (Johra et al., 2023). This spatial resolution allows for a precise examination of how the updated heat exchange algorithms perform in the near-wall boundary layer. While the updated physical kernel inherently alters the wider surface energy balance, this validation focuses exclusively on near-surface air temperature. This targeted scope is driven by the specific nature of the algorithmic update, which directly modifies atmospheric sensible heating rates, and the specific parameters monitored in the available high-resolution field dataset.

By driving both model versions with high-quality, site-specific meteorological forcing and model area info, the current study investigates whether ENVI-met provides sufficient accuracy in modeling air temperature at varying sites near building façades when initialized with rigorous detail. Furthermore, this study examines whether V59, through its corrected heat exchange formulation and code optimizations, yields higher physical accuracy in near-surface air temperature predictions and a higher computational speed compared to V56.

2. Methodology

To quantify the impact of recent algorithmic optimizations, two versions of the ENVI-met model (Section 2.1) were compared against in-situ measurement data. The measurements originate from an open dataset, where air temperatures were measured surrounding an office building in Aalborg, Denmark (Section 2.2). Simulations were conducted with high spatial resolution using Full Forcing boundary conditions derived from a nearby meteorological station to replicate field conditions as accurately as possible (Section 2.3).

2.1. Model versions

The ENVI-met model versions evaluated are.

- Version 5.6 (V56): Represents the baseline with the legacy calculation kernel.
- Version 5.9 (V59): Incorporates computational speed optimizations, the corrected surface-to-air heat exchange formulation and an update of the default heat exchange method between walls/roofs and air.

In V59, a critical refinement was introduced in the calculation of surface-to-air sensible heat exchange to improve the physical accuracy of temperature tendencies in the first atmospheric layer. In previous versions, the heat transfer term governing the air temperature node relied on the squared distance from the surface to the cell center ($dz_h = dz/2$) in the denominator of Eq. (1), with HR as heat rate, K_h as heat exchange coefficient, T_{surf} as surface temperature and T_{air} as air temperature.

$$HR\ [Ks^{-1}] = \frac{K_h\ [m^2 s^{-1}] * (T_{surf} - T_{air})\ [K]}{dz_h{}^2\ [m^2]} \tag{1}$$

This formulation has been corrected in V59 to differentiate between the distance required for the gradient calculation and the volume height required for the thermal mass calculation (Eq. (2)). The updated denominator is calculated as the product of the distance to the cell center (dz_h) and the total vertical extent of the grid cell (dz). Physically, this adjustment ensures that dz_h correctly scales the temperature gradient between the surface and the first air node, while dz appropriately scales the heating rate over the entire air volume of the cell.

$$HR\ [Ks^{-1}] = \frac{K_h\ [m^2 s^{-1}] * (T_{surf} - T_{air})\ [K]}{dz_h * dz\ [m^2]} \tag{2}$$

Besides, with V59, the default heat exchange method between walls/roofs and air was changed from DIN to Monin-Obukhov similarity theory (MOST), which better accounts for the complex interactions between surfaces and atmosphere (Bruse et al., 2023).

2.2. Validation dataset and site Description

The simulation results were validated against a high-resolution microclimate dataset collected by H. Johra and M. Lenoël during the summer of 2022 at Aalborg University, Denmark (57.01° N, 9.97° E; Fig. 1) (Johra, 2023; Johra et al., 2023; Johra and Lenoël, 2023a, 2023b). The study site features a standalone five-storey office building ("AAU-TMV") located in a low-density suburban environment with generally flat terrain (Johra, 2023).

The dataset was selected for this validation due to its high-resolution monitoring of air temperature across distinct microclimates, specifically the shaded Northern façade, the sun-exposed Southern façade, and the exposed rooftop. While a holistic validation of the urban surface energy balance would ideally include in-situ measurements of surface temperatures and MRT, these variables were not monitored in this specific field campaign. Because the critical algorithmic update in V5.9 (Eq. (2)) specifically corrects the volume-height formulation governing the sensible heating rate of the atmospheric grid cells, rather than the surface sensible heat flux itself, validating these high-resolution near-wall air temperatures provides the most direct and mathematically appropriate assessment of the updated physical kernel. Air temperature was measured using calibrated PT100 Resistance Temperature Detectors (RTDs) with an accuracy of ± 0.1 K (Johra, 2019). All sensors were housed in mechanically ventilated, silver-coated tubes to eliminate radiative heating errors (Fig. 2) (Johra and Lenoël, 2023a). Measurements were taken in 2-s intervals and then averaged to 5-min intervals. Temperature profiles were recorded perpendicular to the building envelope at the South façade (SOUTH1 and SOUTH2), the North façade (NORTH), and the dark asphalt Rooftop (ROOF).

At each location, sensors were spaced at distances of 5, 10, 20, 30, 40, 50, 100, and 200 cm from the wall/roof surface (Fig. 2) (Johra and Lenoël, 2023a). Sensor orientation played a critical role in data quality; at the Northern site, tube openings faced East without obstruction (Fig. 1e). Unlike the Southern sites, where Western wall projections and neighboring buildings in the East prevented direct solar intrusion (Fig. 1c), the lack of projection at the Northern site likely allowed direct solar radiation to penetrate the tubes during the low solar altitude angles of the morning. Additionally, the SOUTH2 site was intentionally situated near a building ventilation exhaust (Johra and Lenoël, 2023a), introducing a localized anthropogenic heat source, which cannot yet be implemented in ENVI-met.

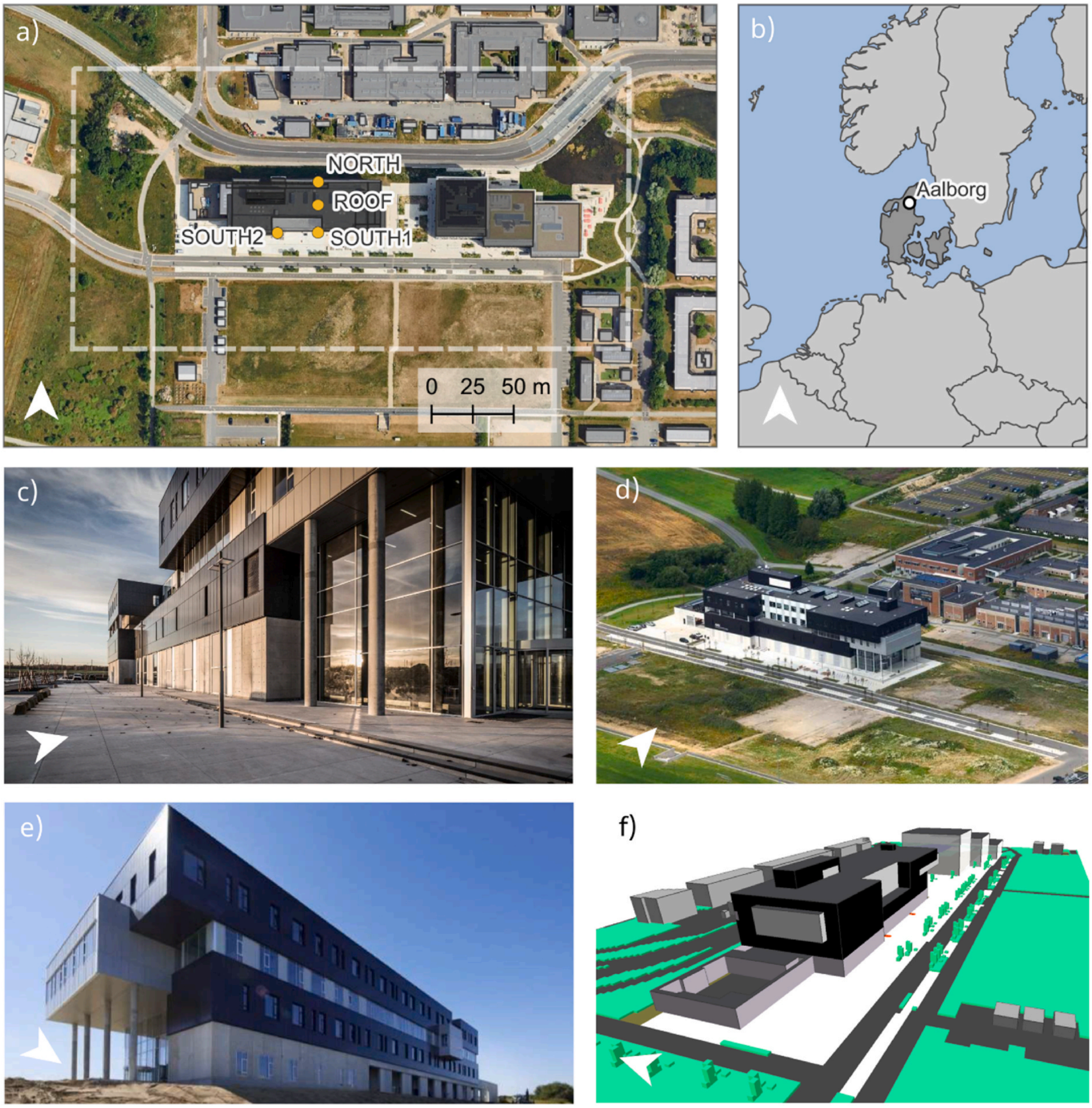

Fig. 1. Detailed site depictions showing a top-down aerial view indicating model area dimensions (white dashed line) and labeled measurement sites (a) (Google Maps, 2026), a map with the position of the site in Aalborg, Denmark made with Natural Earth (b), a photography of the Southern façade of the building (c) (Ronge Fotografi (Johra, 2023)), an aerial view of the entire site where neighboring buildings in the East were yet missing but have been built between taking the aerial imagery and the start of the measurement campaign (d) (Johra, 2023), a photography of the Northern façade of the building (e) (Johra, 2023), and a 3D view of the digitized model area in ENVI-met's editor Spaces showing the Western and Southern façades (f). Figures c), d), e) reprinted from Johra (2023) under a CC BY 4.0 license.

2.3. Simulation settings

Simulation settings, model area configuration, and most relevant database parameters are summarized in Table 1. The model domain was maximized to capture the surroundings while maintaining computational feasibility, utilizing a high horizontal resolution of 1 m, which enables the option of comparing two distances of measurements with the modeling data: Since the field campaign measured at 0.5 m in front of a wall, a horizontal resolution of 1 m directly yields the ideal comparison point of 0.5 m at the center of a grid cell in front of a wall. As further measurement distances only cover 1 m and 2 m, the next modelled grid center distance of 1.5 m is compared to the mean of the 1 m and 2 m measurements. Consequently, field measurements recorded at closer distances (0.1, 0.2, 0.3, and 0.4 m) were excluded from this validation. Since a RANS model inherently cannot resolve thermodynamic gradients at the sub-grid scale, evaluating these near-wall data points would exceed the spatial resolution limits of the 1 m grid. To save computational effort, the vertical resolution was set to 2.5 m with enabled splitting and telescoping. By using splitting option for the lowest grid cell, we get output values for the grid cell center heights of 1.75 m and 2.25 m, which are averaged to be comparable to the measurements at 2 m height. Telescoping is enabled after a model area height of 30 m, while the highest building cell reaches 24 m.

Measurements at the roof site were taken above the 20 m building roof level. The center of the first grid cell above the roof is located at 21.25 m in the model and is hence compared against the 1 m roof measurement height. No further comparisons for other distances are conducted for the ROOF site. Because the vertical grid resolution (2.5 m)

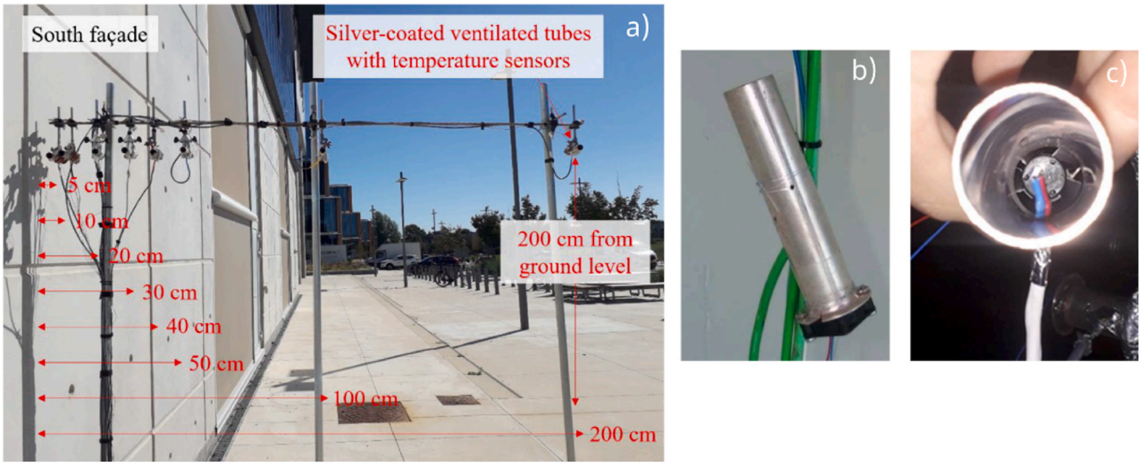

Fig. 2. Measurement setup used at each site with the different measurement distances to the surfaces shown exemplary for SOUTH1 site (a) (Johra et al., 2023), and an exterior view of the silver-coated tubes (b) (Johra and Lenoël, 2023a), containing the PT100 RTDs and a ventilation system for accurate air temperature measurement (c) (Johra and Lenoël, 2023a). Figure a) reprinted from Johra et al. (2023) under a CC BY 3.0 license. Figures b) and c) reprinted from Johra and Lenoël (2023a) under a CC BY 4.0 license.

is coarser than the horizontal resolution (1 m), the model cannot resolve multiple discrete distances within the immediate boundary layer of the roof as it does for the façades. While this differing resolution prevents a direct spatial comparison of near-wall gradients between the roof and the façades, comparing this single vertical node still remains effective for validating the overall diurnal temperature evolution above the roof structure.

The indoor air temperature was held constant at 21 °C, since the building is described as air-conditioned. Building material parameters and layer composition for walls and roofs follow the standard of the Danish building regulation class 2015, which was explicitly used for the construction of this building (Johra, 2023). Albedo values of 0.5 for the walls and 0.1 for the dark roof were provided by the field study documentation (Johra et al., 2023).

The simulation period covers an entire week during summer with varying meteorological conditions. The period of 168 h starting from July 28, 2022, is characterized by several days of clear skies and high solar irradiance to maximize thermal load testing (Fig. 3). An additional criterion for the selection of this period was that field measurement data were almost continuously available for all sites for the entire time. The simulations were driven by Full Forcing, which is the most accurate ENVI-met boundary condition option (Ouyang et al., 2022). Meteorological data for the Full Forcing were derived from the dataset that was provided alongside the air temperature field study data (DAVIS, 2023; Johra and Lenoël, 2023a). For the simulations, all data were taken from a local meteorological station located on the building roof. Prior to simulation, the provided alternative meteorological data sources were rigorously evaluated, including a nearby open-field measurement station and the regional DMI reference station (Tylstrup). However, the nearby open-field station exhibited a pronounced morning warm bias, indicative of compromised solar radiation shielding during low solar altitudes. Conversely, the DMI station provided only air temperature values in hourly temporal resolution, which was considered too coarse for the precise boundary condition forcing in this air temperature validation study. Furthermore, they exhibited a severe nocturnal cooling bias of several Kelvin compared to the local site reality found in the nearby open-field measurement station. Consequently, the 5-min resolution roof station data was selected as the most reliable, continuous baseline, acknowledging that it inherently introduces specific local microclimatic artifacts into the forcing file. The forced parameters for the entire simulation period are displayed in Fig. 3.

Regarding radiative forcing, a standard approximation of 70% direct and 30% diffuse shortwave radiation was applied, as only global shortwave radiation was measured (Boland et al., 2013). This fixed ratio was selected as a robust baseline for the predominantly clear-sky summer conditions to avoid introducing synthetic diurnal noise that unverified dynamic partitioning might cause. Similarly, downwelling longwave radiation measurements were not available. Consequently, the model's internal clear-sky estimation was utilized as the most mathematically stable fallback mechanism. Attempting to artificially generate dynamic longwave radiation profiles without empirical near-site cloud cover data would introduce unverified input uncertainty, obscuring the true performance of the microclimate kernel. Furthermore, given the site's coastal exposure, observed wind speeds fluctuated significantly, occasionally exceeding the optimal stability range of ENVI-met's turbulence model or dropping below the threshold required for efficient CFD resolution. To maintain numerical stability and computational efficiency, input wind speeds were clamped between a lower bound of 1.0 m/s and an upper bound of 3.5 m/s. In the context of ENVI-met, 1.0 m/s effectively represents low-wind conditions where buoyancy dominates, while 3.5 m/s sufficiently emulates strong advective forcing. Although the model can resolve a wider range of velocities, doing so would have disproportionately increased both computation time and the risk of a simulation crash with only marginal gains in thermal accuracy. Crucially, while wind speed magnitudes were constrained, the observed wind directions were incorporated only slightly smoothened to preserve the site-specific advection patterns.

The time zone longitude value of the model area should best be automatically set by the Geodata2ENVImet QGIS plugin or by the model area settings dialog in ENVI-met Spaces. These dialogs set the time zone longitude value for the model area according to the nearest 15° interval of the model area's longitudinal position, i.e. 15° for the 9.97° E position of the current study's area. Furthermore, as ENVI-met always runs without daylight saving hour, input meteorological data from local stations usually needs to be corrected, i.e. from UTC+2 to UTC+1 for the current study.

Both simulations of V56 and V59 were conducted on the same high-performance desktop PC featuring an AMD Ryzen Threadripper Pro 5965WX with 24 CPU/48 logical cores and 512 GB RAM. That allows us to generally investigate if there is a difference in computational speed between the two versions.

3. Results

Before analyzing the physical accuracy of the model, it can be stated that the computational speed improved from ~1383 h simulation time

Table 1
Simulation settings, model area details, and database properties used in the ENVI-met simulations.

		Properties	Values		
Simulation		Start Date and Time (Local)	2022-07-28 04:00		
		Duration [h]	168		
		Meteorological Boundary Conditions	Full Forcing		
		Initial Soil Temperature per layer [°C]	17, 15.7, 14,4, 12		
		Initial Soil Humidity per layer [%]	45, 50, 55, 60		
		Initial Building Surface Temperature [°C]	15		
		Fixed Building Indoor Temperature [°C]	21		
		Output Interval [min]	15 (main)/5 (receptors)		
Model Area		Location Latitude (Lower Left Corner)	57.01° N		
		Location Longitude (Lower Left Corner)	9.97° E		
		Dimensions	340 x 171 x 35		
		Resolutions (X, Y, Z) [m]	1 x 1 x 2.5		
		Nesting Grids	5		
		Lowest Grid Cell Split	Yes		
		Telescoping: Factor and Starting Height	10% above 30 m		
		Height of 3D Model Domain [m]	248.74		
		Model Rotation out of grid north	0°		
Database	**Soil**	Pavement surface albedo	0.5		
		Street surface albedo	0.2		
	Material		*Concrete (C)*	*Insulation (I)*	*Bitumen (B)*
		Albedo	0.5	0.5	0.1
		Specific Heat Capacity	1000	840	1000
		Thermal conductivity	1.8	0.038	0.7
		Density	2400	40	2100
	Wall		*Wall*		*Roof*
		Layers (outer to inner)	C, I, C		B, I, C
		Layer Thickness [cm]	10, 25, 10		2, 35, 20

for V56 to ~455 h for V59, which is approximately three times faster. While these numbers give a rough estimation of the performance increase, run times generally vary strongly between differing hardware setups and must be interpreted with caution.

To assess the general modeling accuracy and investigate systemic improvements between versions, the modelled data for the entire simulation period across all sites were first aggregated into scatter plots providing general statistical metrics with the coefficient of determination (R^2) and Root Mean Square Error (RMSE) (Fig. 4). It is important to note that the entire, unmanipulated dataset was retained for these aggregated calculations, including data from periods and locations affected by the site-specific complexities introduced in Section 2.2. Retaining all data points ensures a rigorous, conservative assessment of overall model performance, with specific physical discrepancies treated as contextual outliers in the subsequent discussion (Section 4).

The baseline simulation (V56) exhibits a general systemic overestimation, combined with a wider spread of residuals (RMSE = 0.89 K). The regression slope of 0.98 further indicates a slight tendency to underestimate the absolute peak temperature extremes while overestimating the baseline. The updated model (V59) demonstrates a significantly tighter clustering of data points around the identity line, effectively reducing the systemic bias. The overall RMSE across all sites drops to 0.78 K, and the coefficient of determination increases to $R^2 = 0.95$. This reduction in scatter validates that the code optimizations and physical corrections in V59 yield a more robust prediction of the urban microclimate across varying boundary conditions.

While the aggregated data validates the overall reliability of both versions, the temporal evolution of air temperatures (Fig. 5,Fig. 6) and the detailed statistical metrics (Table 2,Table 3) reveal critical site-specific nuances. By introducing Mean Bias Error (MBE) and Mean Absolute Error (MAE) stratified into daytime and nighttime periods, the specific algorithmic strengths of V59 become apparent.

As shown in Fig. 5 and Table 2, the general agreement at the Roof level (1 m) is particularly strong, with both versions achieving an R^2 of 0.97. However, V56 exhibits a slightly higher RMSE (0.64 K) and MAE (0.50 K) compared to the updated V59 (RMSE = 0.58 K, MAE = 0.46 K). Furthermore, the stratified MBE values reveal a systemic tendency: across most sites (ROOF, NORTH, SOUTH1), the model exhibits a positive MBE, indicating a general warm bias. This is most pronounced during the nighttime periods, a thermodynamic discrepancy that is analyzed further in Section 4.2.

At the North façade (1.5 m), V56 shows a strong tendency to deviate during peak temperatures, resulting in a lower R^2 of 0.89 and an overall MBE of 0.46 K. In contrast, V59 improves the correlation to $R^2 = 0.91$ and reduces the MBE to 0.37 K, suggesting that the updated surface-to-air heat transfer formulation captures the thermal dynamics in shaded environments slightly better. Similar improvements are observed at the sun-exposed SOUTH1 façade (1.5 m), where V59 reduces the overall MBE from 0.50 K to 0.32 K. However, a highly notable exception to this systemic warming trend occurs at the SOUTH2 site. Here, V59 exhibits a negative MBE (−0.18 K), indicating a low but persistent cold bias. The physical cause of this localized statistical anomaly is detailed in Section 4.3.

The near-wall comparisons (0.5 m distance), depicted in Fig. 6 and quantified in Table 3, further corroborate these findings while highlighting the strength of the updated algorithms. At the SOUTH1 site, V59 cuts the overall MBE almost in half (from 0.41 K to 0.23 K) and achieves a very high correlation ($R^2 = 0.96$) alongside a slightly lower RMSE (0.72 K) compared to V56 (0.85 K). This indicates that changing the default for the façade calculation to the MOST approach in V59 is particularly effective in resolving the steeper temperature gradients found in the immediate vicinity of sun-lit surfaces. The underlying thermodynamic mechanisms driving this distinct localized improvement at the sun-exposed façade are analyzed in Section 4.4.

4. Discussion and limitations

While the validation results demonstrate a strong agreement between model results and in-situ measurements, several limitations regarding the measurement setup and model parametrization must be addressed to contextualize the results and remaining discrepancies. The discussion covers measurement artifacts (Section 4.1), the influence of boundary conditions (Section 4.2), simplifications regarding geometries and materials (Section 4.3), and the general model performance assessment (Section 4.4).

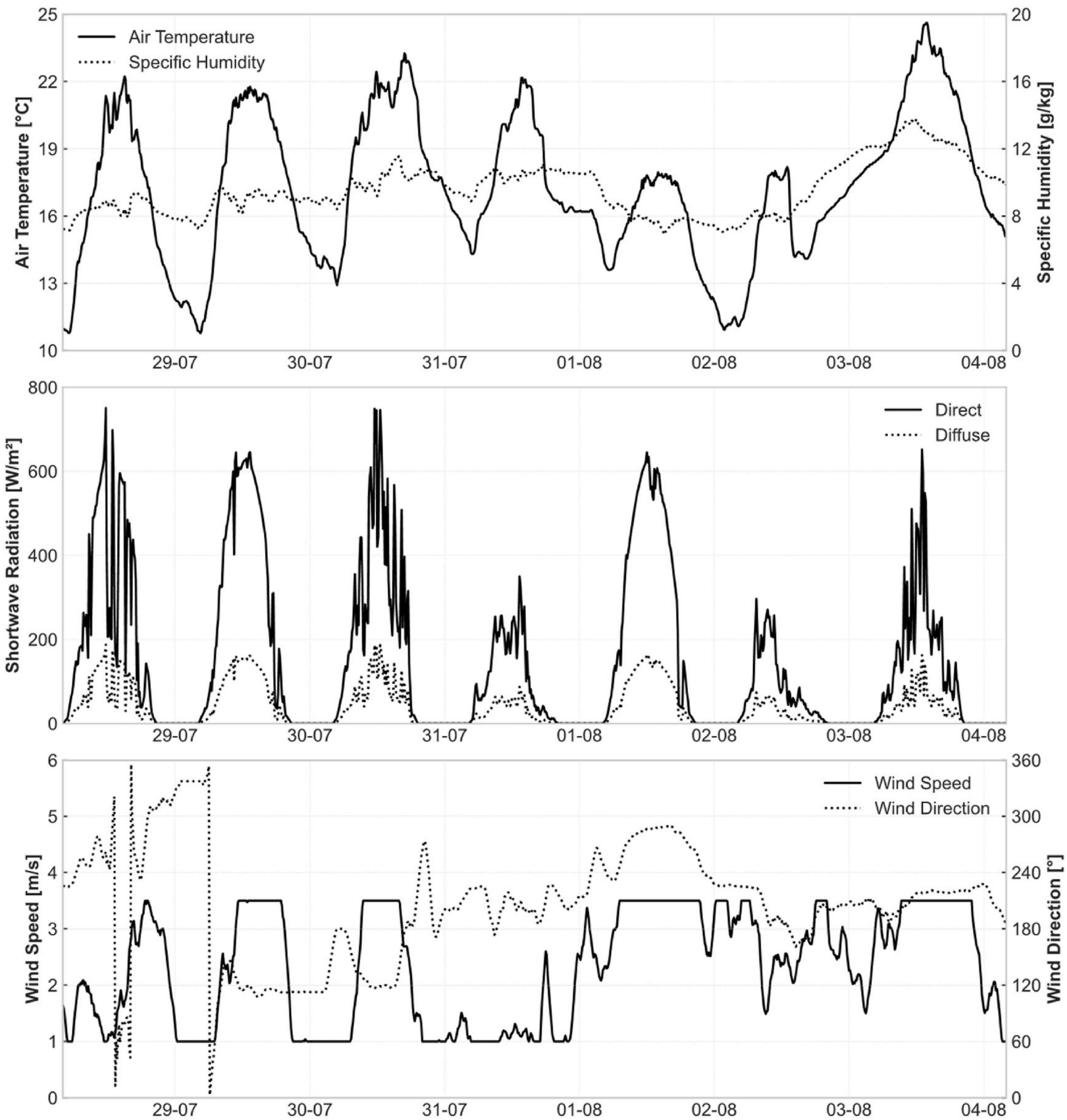

Fig. 3. Meteorological forcing parameters applied to the simulation domain for the period of July 28 to August 04, 2022. The panels display the diurnal evolution of air temperature and specific humidity (top), global shortwave radiation approximated as 70% direct and 30% diffuse components (middle), and wind speed and direction (bottom).

4.1. Measurement artifacts

A primary source of deviation, particularly during morning hours, can be attributed to the temperature sensor design. Although the sensors were housed in silver-coated, ventilated tubes, the lack of a wall projection on the Northern site allowed direct solar radiation to penetrate the tube openings during periods of low solar altitude, particularly in the morning hours. This likely induced radiative heating of the sensor element – an artifact not accounted for by the model, which assumes idealized air temperature readings. This artifact is only visible for days with clear sky conditions during morning hours, exemplary displayed for the 31-07-2022 in Fig. 7. While representing only short timeframes of error, they are still negatively affecting the statistical metrics for the model performance assessment.

Although peak air temperatures under clear-sky conditions were generally well-reproduced, the model overestimated temperatures at the NORTH site on July 28th, 29th, and August 1st. This discrepancy could be attributable to the façade geometry; as shown in Fig. 1e, an arcade structure spans half the Northern façade. While it is not extending up the measurement site, the arcade's shaded volume presumably traps a pocket of cooler air, the influence of which appears to be modulated by wind direction. The well-captured days correlated with prevailing winds from the South and South-West, while the days exhibiting overestimation were dominated by Easterly and (North-)Westerly flows. These distinct patterns could have governed the advection of the cool arcade air toward the sensor, hence affecting the measurements. However, this arcade structure was excluded from the final simulation domain. Preliminary test runs indicated that the semi-enclosed geometry caused numerical instability, specifically preventing the solver from converging on a stable wind flow field within these stagnant air volumes.

4.2. Boundary conditions

The smoothing and capping of wind speeds in the simulation input could have introduced some uncertainty. High wind speeds observed at the coastal model area site were capped at 3.5 m/s to ensure numerical stability within the CFD domain. This artificial reduction in wind

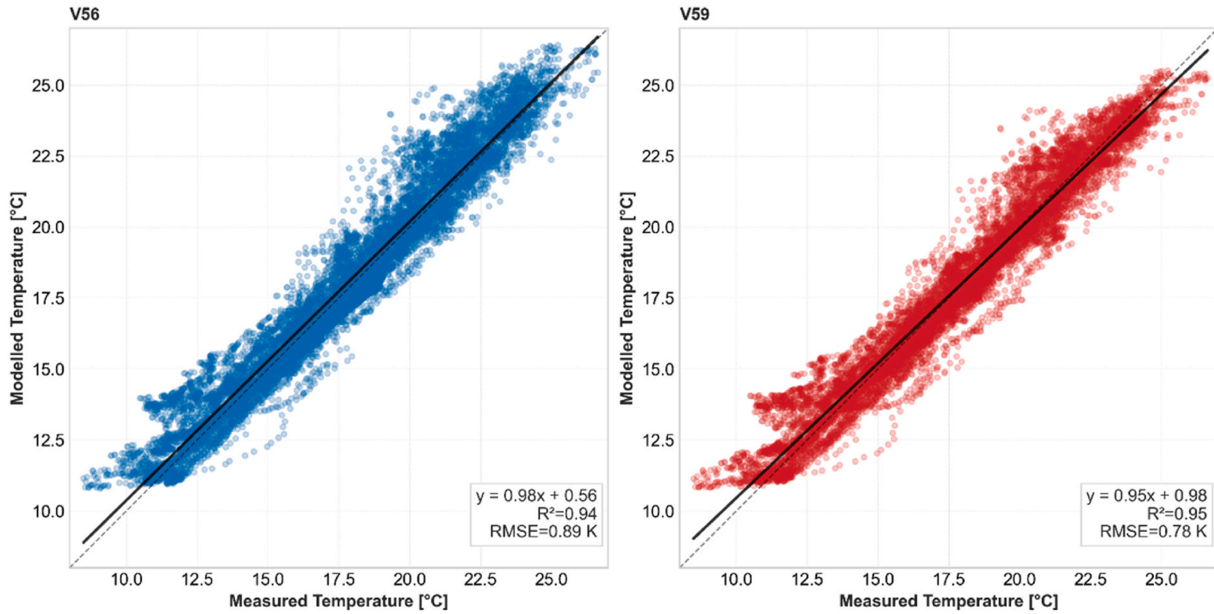

Fig. 4. Aggregated scatter plots of modelled versus measured air temperatures. The data combines all measurement sites and time steps for the entire simulation period. The left panel (blue markers) shows the performance of V56, while the right panel (red markers) shows V59. The solid black line indicates the linear regression, and the dashed grey line represents the 1:1 identity line. (For interpretation of the references to color in this figure legend, the reader is referred to the Web version of this article.)

velocity likely led to an underestimation of convective heat removal (advection) in the model, potentially causing a light warm bias during windy periods. On the contrary, the lower boundary of 1 m/s could have caused a light cold bias during calm-wind situations.

Furthermore, the radiative forcing relied on several approximations. Since only global shortwave radiation was measured, the ratio of direct to diffuse radiation was estimated at a fixed 70/30 split. This simplification fails to capture dynamic changes in cloud cover opacity, leading to inaccuracies in the surface energy budget. Additionally, longwave radiation was not explicitly forced as measurements were not available and was hence estimated by the model based on clear-sky assumption. However, as there are several simulation periods with significantly reduced shortwave radiation values, there must have been cloud cover in reality. The model hence underestimated the incoming longwave radiation for the cloudy periods, which can be a larger source of error (Schöneberger et al., 2025).

A specific discrepancy observed during the first two nights of the simulation, where the model exhibited a persistent nocturnal warm bias of approximately 2 K across all sites (quantitatively reflected by the universally positive nocturnal MBE values in Table 2 andTable 3), can be directly attributed to the thermodynamic environment of the forcing data source. The meteorological input was derived from a roof-level station situated over a dark roof (albedo = 0.1). During the clear-sky daytime hours, this high thermal mass structure absorbed significant solar radiation. At night, the stored energy was gradually released back into the near-surface atmosphere. Because nocturnal wind speeds were generally low, reaching the 1.0 m/s minimum stability threshold, convective cooling and advective mixing were highly restricted at the roof level. Consequently, a localized layer of warm air stagnated over the roof structure. This combined thermodynamic mechanism caused the air temperatures measured at the forcing station to remain significantly warmer than the ambient air at street level. By utilizing these elevated roof-level temperatures as the global meteorological boundary condition, this localized 2 K warm bias was inadvertently propagated throughout the entire model domain, leading to the observed overestimations at the near-wall NORTH and SOUTH sites.

The dominance of this localized roof-level heating explicitly addresses an apparent thermodynamic contradiction regarding the model's longwave radiation forcing. As previously noted, estimating missing downwelling longwave data using a clear-sky assumption theoretically promotes nocturnal overcooling due to an underestimated radiative budget during cloudy periods. However, the simulation exhibited a net warm bias. This indicates that the direct, continuous injection of sensible heat from the roof's thermal mass into the stagnant air layer surrounding the weather station overpowered the generalized radiative cooling deficit. Essentially, because the applied meteorological boundary conditions were artificially saturated with localized sensible heat of the roof station measurements, they overrode the model's baseline physical tendency to overcool under the clear-sky approximation.

4.3. *Geometric and material simplifications*

The digital representation of the building and its surroundings inherently requires geometric and material simplifications. While physical material properties such as specific heat capacity and thermal conductivity were not determined through site-specific lab tests, they were not derived from generic literature defaults. Instead, the building material parameters and layer compositions for walls and roofs were modelled strictly according to the Danish building regulation class 2015, which was explicitly the standard used for the construction of this specific building. While in-situ aging, moisture content, or construction tolerances might introduce minor deviations from these nominal values, utilizing the precise regulatory design specifications represents the highest achievable parameter accuracy. Consequently, a dedicated sensitivity analysis of these specific material properties was deemed outside the scope of this validation.

Geometrically, the model omits architectural details like the arcades mentioned in Section 4.1. Furthermore, assuming a static indoor temperature of 21 °C represents a simplification of the building's thermal boundary conditions. While this accurately reflects the target setpoint of the air-conditioned building, it inherently neglects minor dynamic indoor temperature fluctuations. More critically, the anthropogenic heat ejected by the HVAC system to maintain this 21 °C setpoint, specifically at a ventilation outlet located near the SOUTH2 site, could not be dynamically modelled. The absence of this anthropogenic sensible heat directly explains the statistical anomaly observed at this location in

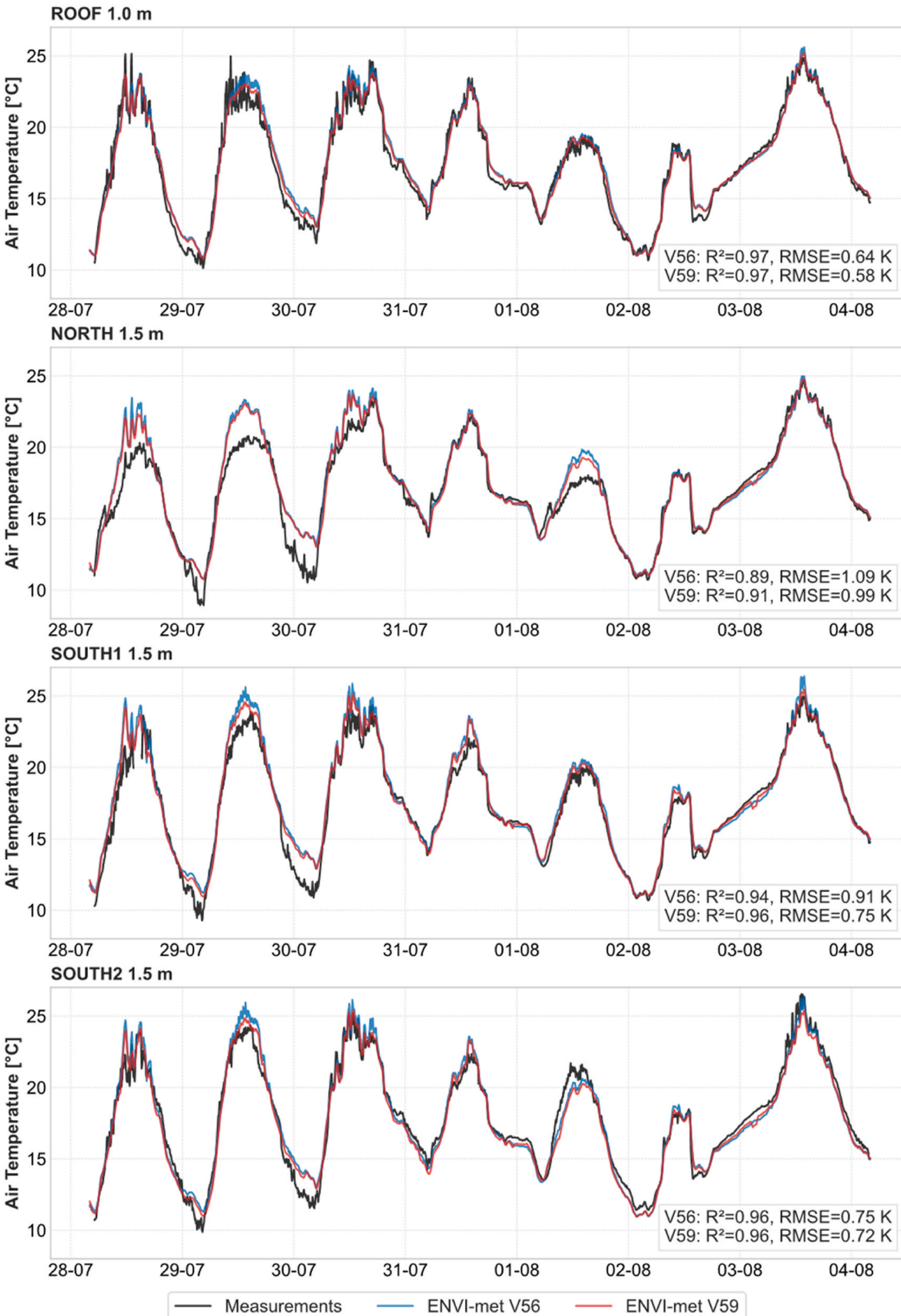

Fig. 5. Temporal comparison of the evolution of modelled and measured air temperatures at 1.5 m distance from the façade (1.0 m for the Roof) for the North, South, and Roof sites. Black lines represent in-situ measurements, blue lines represent V56, and red lines represent V59. (For interpretation of the references to color in this figure legend, the reader is referred to the Web version of this article.)

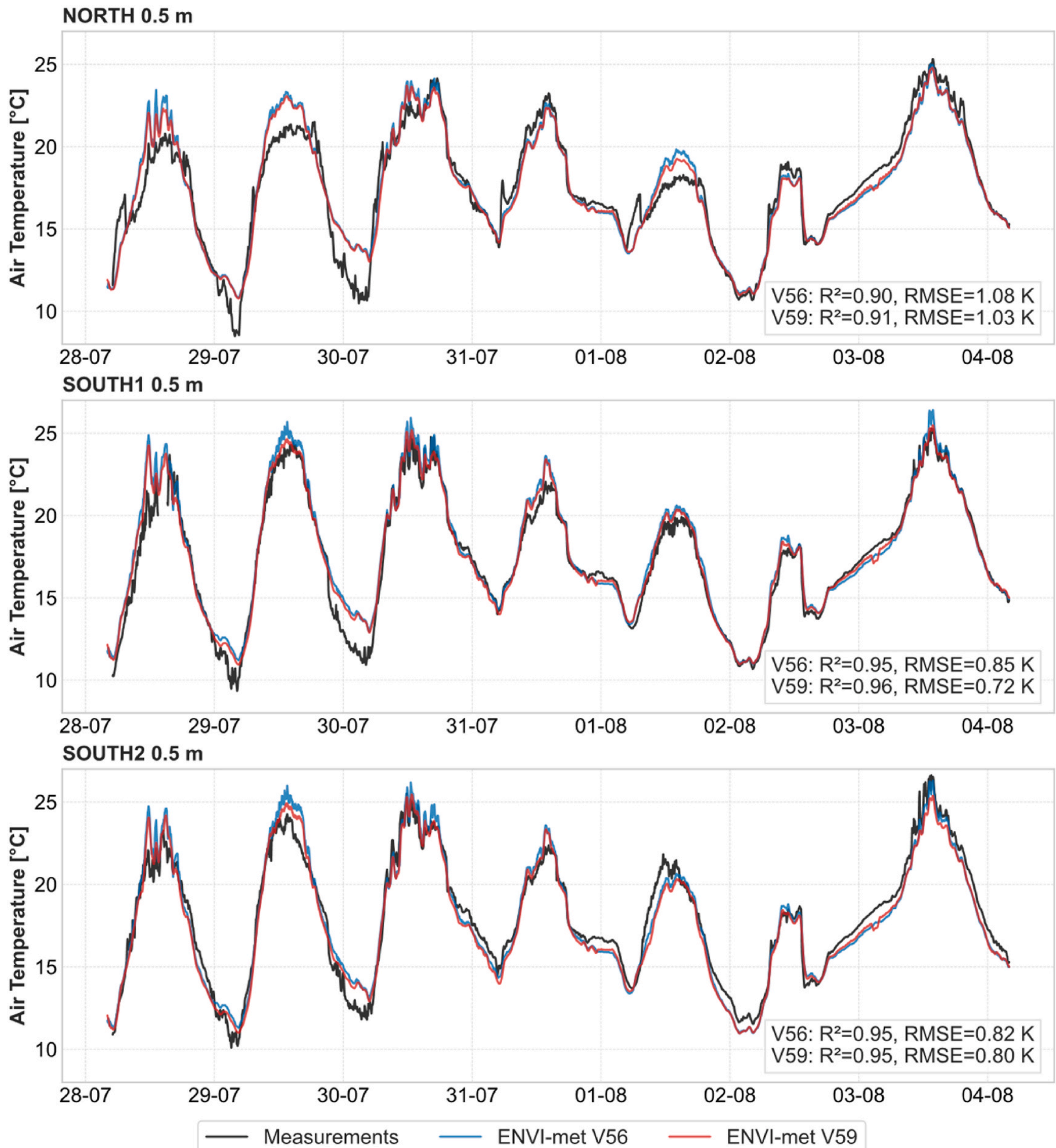

Fig. 6. Temporal comparison of the evolution of modelled and measured air temperatures at 0.5 m distance from the façade for the North and South sites. The color coding follows the previous figure: Measurements (black), V56 (blue), and V59 (red). (For interpretation of the references to color in this figure legend, the reader is referred to the Web version of this article.)

Section 3. As shown in Table 2 andTable 3, SOUTH2 is the only measurement site exhibiting a systemic cold bias (negative MBE). Because the model lacks this continuous heat source, it correctly simulates a cooler, unadulterated natural environment, resulting in the observed underestimation.

Additionally, the terrain was modelled as flat to facilitate the advantages of the splitting option, ignoring the slope of around 4 m height on the Northern side which could influence local airflow patterns and could be an additional explanation for the larger discrepancies that were found at the NORTH site compared to the other sites.

4.4. General model performance assessment

When analyzing the overall performance of both versions achieving a R^2 of >0.94 and a RMSE of <1 K, the model performance remains surprisingly robust despite the previously discussed constraints. However, distinct open issues regarding the model's capabilities persist.

First, discrepancies remain visible during periods of full solar exposure in the daytime, as well as during nocturnal cooling phases. While there are several possible explanations for these observations discussed in the previous Sections 4.1 to 4.3, some uncertainty regarding these specific discrepancies persists.

Second, the model did not fully reproduce the spatial variability observed in the field data. While we find ~1.5 K lower air temperatures at the Southern façade compared to the Northern façade during noon of the clear-sky day July 29th (Fig. 8), the differences were not as pronounced as they were in the in-situ measurements (~2.5 K). This spatial compression is the direct result of the localized geometric simplifications discussed previously: specifically, the overestimation of the North façade due to the omitted cooling arcade (Section 4.1) combined with the underestimation of the South façade due to the absent HVAC exhaust (Section 4.3).

Furthermore, the model struggled to resolve the strong temperature gradients near the building envelope. There was no larger difference

Table 2
Statistical metrics for the comparison between modelled and measured air temperatures at 1.5 m distance from the façade (1.0 m for the Roof) for the North, South, and Roof sites.

Site	Type	Period	R^2	RMSE	MBE	MAE
ROOF 1.0m	V56	Overall	0.97	0.64	0.25	0.5
		Day	0.95	0.67	0.2	0.52
		Night	0.94	0.58	0.34	0.47
	V59	Overall	0.97	0.58	0.12	0.46
		Day	0.96	0.63	0.03	0.49
		Night	0.96	0.49	0.26	0.4
NORTH 1.5m	V56	Overall	0.89	1.09	0.46	0.73
		Day	0.81	1.16	0.55	0.8
		Night	0.86	0.96	0.32	0.6
	V59	Overall	0.91	0.99	0.37	0.66
		Day	0.86	1.01	0.41	0.72
		Night	0.87	0.94	0.31	0.56
SOUTH1 1.5m	V56	Overall	0.94	0.91	0.5	0.64
		Day	0.91	0.92	0.61	0.69
		Night	0.88	0.9	0.31	0.56
	V59	Overall	0.96	0.75	0.32	0.51
		Day	0.95	0.72	0.36	0.51
		Night	0.9	0.8	0.26	0.49
SOUTH2 1.5m	V56	Overall	0.96	0.75	0.01	0.6
		Day	0.95	0.75	0.08	0.57
		Night	0.91	0.76	−0.1	0.65
	V59	Overall	0.96	0.72	−0.18	0.58
		Day	0.95	0.73	−0.18	0.57
		Night	0.92	0.7	−0.18	0.6

Table 3
Statistical metrics for the comparison between modelled and measured air temperatures at 0.5 m distance from the façade for the North and South sites.

Site	Type	Period	R^2	RMSE	MBE	MAE
NORTH 0.5m	V56	Overall	0.9	1.08	0.09	0.82
		Day	0.85	1.09	0.05	0.88
		Night	0.85	1.08	0.16	0.73
	V59	Overall	0.91	1.03	0	0.78
		Day	0.87	1	−0.08	0.83
		Night	0.85	1.06	0.14	0.69
SOUTH1 0.5m	V56	Overall	0.95	0.85	0.41	0.6
		Day	0.94	0.82	0.5	0.6
		Night	0.88	0.9	0.25	0.58
	V59	Overall	0.96	0.72	0.23	0.48
		Day	0.96	0.66	0.26	0.46
		Night	0.91	0.8	0.19	0.52
SOUTH2 0.5m	V56	Overall	0.95	0.82	−0.1	0.69
		Day	0.93	0.81	0	0.63
		Night	0.89	0.84	−0.28	0.78
	V59	Overall	0.95	0.8	−0.3	0.67
		Day	0.94	0.8	−0.26	0.64
		Night	0.9	0.8	−0.37	0.73

between the modelled temperatures at 0.5 m and 1.5 m distance from the wall, whereas the measurement data showed clear distinctions (Fig. 5,Fig. 6). This behavior was observed regardless of whether the legacy DIN approach (V56) or the MOST method (V59) was used as default wall-air heat exchange algorithm, suggesting a possible need for further investigation into alternative parameterization approaches for near-wall microclimates.

However, these discrepancies are intrinsically linked to the structural limitations of Reynolds-Averaged Navier-Stokes (RANS) turbulence models. RANS equations rely on time-averaging the turbulent flow field, which inherently struggles to resolve instantaneous, fine-scale eddies near solid boundaries. Furthermore, with only two 1-m grid cells spanning the 2 m zone adjacent to the façade, the calculation is highly susceptible to numerical diffusion. This discretization error artificially increases the mixing of scalar quantities between adjacent computational nodes. Consequently, the sharp micro-scale thermal gradients observed in the field data are numerically smoothed out, resulting in the almost homogeneous modelled temperature field across the 0.5 m and 1.5 m nodes. Achieving a grid resolution fine enough to mitigate this diffusion is currently computationally prohibitive for domain-scale urban microclimate modeling, meaning the high spatial resolution of the validation dataset slightly exceeded the effective resolving power of this class of models.

Third, while V59 demonstrated slightly superior metrics compared to V56, the improvement was not drastic. This is largely because the baseline version (V56) already performed with high reliability. Nevertheless, V59 succeeded in reducing the RMSE and improving the correlation, validating the utility of the code updates. While a formal quantitative attribution analysis isolating each algorithmic change is constrained by the integrated, compiled nature of the ENVI-met version releases, the observed performance improvements can be logically linked to the specific V5.9 updates. The roughly three-fold decrease in simulation runtime is a direct consequence of the backend code optimizations. Furthermore, the general reduction in aggregated RMSE across all measurement sites is primarily attributable to the corrected sensible heating rate formulation (Eq. 2), which globally improves the physical consistency of the atmospheric volume-height calculations. Additionally, the localized enhancements – specifically the exceptionally high correlation and reduced error observed at the 0.5 m distance of the sun-exposed SOUTH1 façade – strongly suggest that enabling the Monin-Obukhov Similarity Theory (MOST) as the default wall-to-air heat exchange algorithm is highly effective at resolving the steeper temperature gradients associated with strong thermal forcing at the building envelope. Conversely, the improvements at the shaded Northern façade are more limited because the buoyancy forces and convective heat transfers are significantly weaker, meaning the differences between the legacy DIN approach and the updated MOST approach are less pronounced.

Finally, this study presents several general limitations, primarily its exclusive focus on air temperature. While previous validation efforts frequently evaluated humidity, wind speed, and/or MRT alongside air temperature (Liu et al., 2021), these studies typically rely on standard street canyon or courtyard measurements. In contrast, the present study specifically addresses the gap in validating near-façade air temperature predictions. Consequently, the absence of field measurements for other thermodynamic variables precluded a holistic validation of outdoor thermal comfort parameters. Furthermore, the validation was geographically and temporally constrained to a single site in a specific climate over one summer week, though it successfully captured diverse sensor locations and meteorological conditions. To further verify the robustness of ENVI-met's parameterizations in the newest version, future research must expand validation efforts across other climatic zones, seasons, parameters, and urban morphologies.

5. Conclusion

This study presented a multi-site, 7-day validation of the ENVI-met microclimate model, comparing the legacy Version 5.6 against the updated Version 5.9. The validation was conducted using a high-resolution dataset of air temperatures measured around a standalone office building in Aalborg, Denmark, covering diverse conditions including shaded, sun-lit, and roof-level environments. Results demonstrate that ENVI-met predicts urban air temperatures with high accuracy when initialized with high-quality, site-specific meteorological forcing and model area info. The updated V59 slightly outperformed the legacy version V56 in two critical areas.

1. Physical Accuracy: The correction of the surface-to-air sensible heat exchange formulation and enabling the MOST approach as default for façade heat exchange calculations resulted in a closer absolute fit to measurements. V59 reduced the overall RMSE to 0.78 K, increased R^2 to 0.95 across all sites, and effectively lowered the systemic warm bias (MBE) across the temporal phases. Improvements were

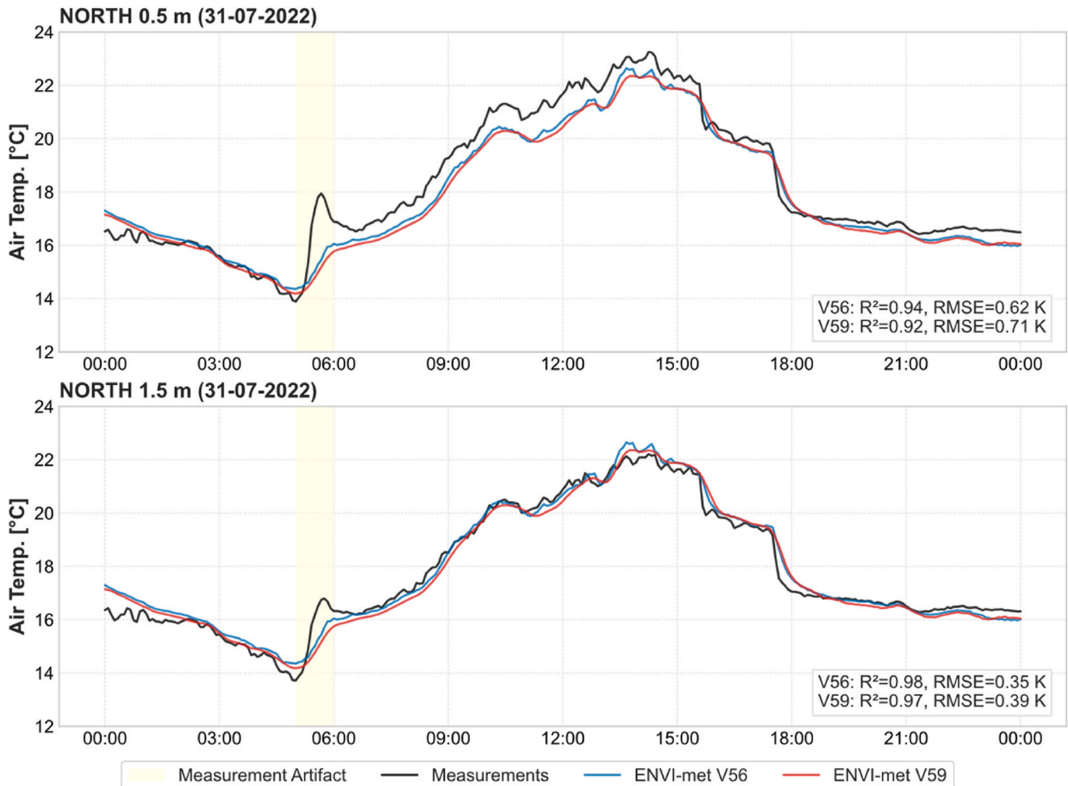

Fig. 7. Temporal comparison of the evolution of modelled and measured air temperatures at 0.5 m and 1.5 m distance from the façade for the North site. The color coding follows the previous figures: Measurements (black), V56 (blue), and V59 (red) with an additional yellow shading between 05:00 and 06:00 to highlight a measurement artifact. (For interpretation of the references to color in this figure legend, the reader is referred to the Web version of this article.)

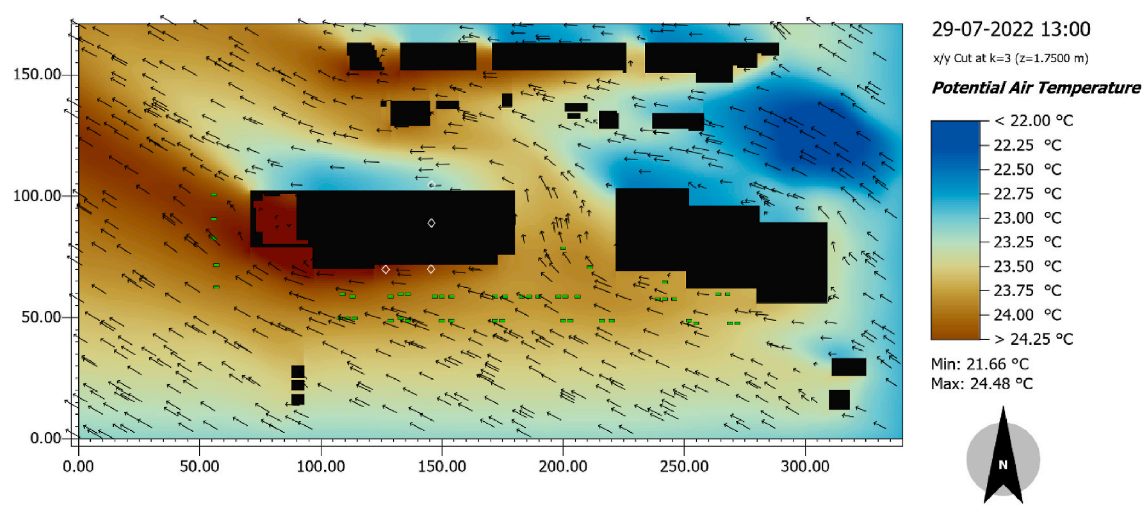

Fig. 8. Air temperature distribution for 29-07-2022 13:00 for the height level of 1.75 m with blue colors indicating lower temperatures and red colors indicating higher temperatures as well as black arrows depicting local wind vectors. Hollow white diamonds highlight measurement site locations. (For interpretation of the references to color in this figure legend, the reader is referred to the Web version of this article.)

particularly pronounced in resolving thermal dynamics at the sun-exposed South façade, where V59 achieved an R^2 of 0.97.
2. Computational Efficiency: Code optimizations in V59 reduced the simulation runtime for the 7-day period roughly by a factor of three.

Despite these improvements, limitations remain regarding the simulation of near-surface gradients (0.5 m vs. 1.5 m) and the dependency on accurate local forcing data to minimize nocturnal biases. The combination of refined physical parameterizations and significantly reduced computational cost demonstrates that ENVI-met V5.9 is a highly capable tool for assessing near-surface air temperatures under the temperate summer conditions evaluated in this study. While its broader, global applicability for urban design interventions remains to be fully verified, these algorithmic improvements represent a meaningful advancement for high-resolution microclimate modeling. Moving forward, the findings from this version comparison highlight clear pathways for future microclimate model optimizations. Specifically, the persistent challenge of resolving sharp thermal gradients within the immediate near-wall boundary layer (0.5 m to 1.5 m) underscores the need for advanced parameterization approaches that can better account for sub-grid scale processes in RANS-based models. Furthermore, while the current study provides robust validation for a temperate summer scenario, establishing the global applicability of the V5.9 kernel necessitates future validation efforts across diverse climatic zones, distinct seasonal variations, other relevant parameters, and more complex urban morphologies.

CRediT authorship contribution statement

Tim Sinsel: Conceptualization, Data curation, Formal analysis, Investigation, Methodology, Project administration, Software, Supervision, Validation, Visualization, Writing – original draft, Writing – review & editing. **Peer Schöneberger:** Software, Validation, Visualization, Writing – review & editing. **Helge Simon:** Conceptualization, Formal analysis, Project administration, Writing – review & editing. **Michael Bruse:** Project administration, Resources, Writing – review & editing.

Declaration of competing interest

The authors declare the following financial interests/personal relationships which may be considered as potential competing interests: Tim Sinsel reports a relationship with One Click LCA Oy that includes: consulting or advisory. Helge Simon reports a relationship with One Click LCA Oy that includes: consulting or advisory. If there are other authors, they declare that they have no known competing financial interests or personal relationships that could have appeared to influence the work reported in this paper.

Data availability

Data will be made available on request.

References

Aleksandrowicz, O., Saroglou, T., Pearlmutter, D., 2023. Evaluation of summer mean radiant temperature simulation in ENVI-met in a hot Mediterranean climate. Build. Environ. 245, 110881. https://doi.org/10.1016/j.buildenv.2023.110881.

Anders, J., Maronga, B., 2025. Urban microscale simulations based on a local climate zone wizard: concept and validation using the PALM model system. Urban Clim. 63, 102576. https://doi.org/10.1016/j.uclim.2025.102576.

Barnstorf, P., Alves, F., Vale, C., 2023. Reflexions on an ENVI-met operation-methodology case study. U.Porto Journal of Engineering 9, 16–99. https://doi.org/10.24840/2183-6493_009-002_001949.

Boland, J., Huang, J., Ridley, B., 2013. Decomposing global solar radiation into its direct and diffuse components. Renew. Sustain. Energy Rev. 28, 749–756. https://doi.org/10.1016/j.rser.2013.08.023.

Bruse, M., Simon, H., Sinsel, T., 2023. Development and implementation of a high-resolution dynamical wall and roof model for ENVI-met Part 1: general model design and non-vegetated walls and roofs. https://doi.org/10.13140/RG.2.2.29309.95207.

Bruse, M., Fleer, H., 1998. Simulating surface-plant-air interactions inside urban environments with a three dimensional numerical model. Environ. Model. Software 13, 373–384.

DAVIS, 2023. Online Weather Observations - Thomas Manns Vej 23. Department of Civil Engineering, Aalborg University.

Detommaso, M., Costanzo, V., Nocera, F., 2021. Application of weather data morphing for calibration of urban ENVI-met microclimate models. Results and critical issues. Urban Clim. 38, 100895. https://doi.org/10.1016/j.uclim.2021.100895.

Dey, S., Joshi, Y., 2022. Recent progress and challenges in microscale urban heat modeling and measurement for urban engineering applications. J. Therm. Sci. Eng. Appl. 15. https://doi.org/10.1115/1.4056054.

Eingrüber, N., Korres, W., Löhnert, U., Schneider, K., 2023. Investigation of the ENVI-met model sensitivity to different wind direction forcing data in a heterogeneous urban environment. In: Advances in Science and Research. Presented at the EMS Annual Meeting: European Conference for Applied Meteorology and Climatology 2022 -. Copernicus GmbH. https://doi.org/10.5194/asr-20-65-2023, 65–71.

Elraouf, R.A., Elmokadem, A., Megahed, N., Eleinen, O.A., Eltarabily, S., 2022. Evaluating urban outdoor thermal comfort: a validation of ENVI-met simulation through field measurement. J. Build. Perform. Simul. 15, 268–286. https://doi.org/10.1080/19401493.2022.2046165.

Google Maps, 2026. Google Satellite.

Hatvani-Kovacs, G., Bush, J., Sharifi, E., Boland, J., 2018. Policy recommendations to increase urban heat stress resilience. Urban Clim. 25, 51–63. https://doi.org/10.1016/j.uclim.2018.05.001.

Huttner, S., 2012. Further Development and Application of the 3D Microclimate Simulation ENVI-met (Phd Thesis). Johannes Gutenberg-University Mainz.

Jänicke, B., Milošević, D., Manavvi, S., 2021. Review of user-friendly models to improve the urban micro-climate. Atmosphere 12. https://doi.org/10.3390/atmos12101291.

Johra, H., 2019. Long-Term Stability and Calibration of the Reference Thermometer ASL F200 (Report), Long-Term Stability and Calibration of the Reference Thermometer ASL F200. Department of Civil Engineering, Aalborg University, Aalborg. https://doi.org/10.54337/aau328894425.

Johra, H., 2023. General Study case description of TMV 23: a multi-storey office building and living lab in Denmark (Report), general Study case description of TMV 23: a multi-storey office building and living lab in Denmark. Department of the Built Environment. Aalborg University, Aalborg. https://doi.org/10.54337/aau511019002.

Johra, H., Lenoël, M., Jensen, R.L., Larsen, O.K., 2023. Outdoor micro-climate: air temperature measurements around an office building in Denmark during summer. In: Journal of Physics: Conference Series. IOP Publishing, 102011.

Johra, H., Lenoël, M., 2023a. Experimental Setup Description and Raw Data from the Micro-climate Measurement Campaign of the Outdoor Air Temperature Around an Office Building in Denmark During Summer.

Johra, H., Lenoël, M., 2023b. Micro-climate measurement campaign of the outdoor air temperature around an office building in Denmark during the summer 2022. https://doi.org/10.5278/53746020-c357-420e-9bf8-5fc8aea31f77.

Lam, C.K.C., Lee, H., Yang, S.-R., Park, S., 2021. A review on the significance and perspective of the numerical simulations of outdoor thermal environment. Sustain. Cities Soc. 71, 102971. https://doi.org/10.1016/j.scs.2021.102971.

Lieber, J., Chen, X., Chen, L., Yang, J., 2025. Comparative analysis of microclimate simulations: assessing the single-layer urban canopy model and ENVI-met in Hong Kong. Urban Clim. 64, 102621. https://doi.org/10.1016/j.uclim.2025.102621.

Lindberg, F., Grimmond, C.S.B., Gabey, A., Huang, B., Kent, C.W., Sun, T., Theeuwes, N. E., Järvi, L., Ward, H.C., Capel-Timms, I., Chang, Y., Jonsson, P., Krave, N., Liu, D., Meyer, D., Olofson, K.F.G., Tan, J., Wästberg, D., Xue, L., Zhang, Z., 2018. Urban Multi-scale Environmental Predictor (UMEP): an integrated tool for city-based climate services. Environ. Model. Software 99, 70–87. https://doi.org/10.1016/j.envsoft.2017.09.020.

Lindberg, F., Holmer, B., Thorsson, S., 2008. Solweig 1.0 – modelling spatial variations of 3D radiant fluxes and mean radiant temperature in complex urban settings. Int. J. Biometeorol. 52, 697–713. https://doi.org/10.1007/s00484-008-0162-7.

Liu, D., Hu, S., Liu, J., 2020. Contrasting the performance capabilities of urban radiation field between three microclimate simulation tools. Build. Environ. 175, 106789. https://doi.org/10.1016/j.buildenv.2020.106789.

Liu, S., Middel, A., Fang, X., Wu, R., 2024. ENVI-met model performance evaluation for courtyard simulations in hot-humid climates. Urban Clim. 55, 101909. https://doi.org/10.1016/j.uclim.2024.101909.

Liu, Z., Cheng, W., Jim, C.Y., Morakinyo, T.E., Shi, Y., Ng, E., 2021. Heat mitigation benefits of urban green and blue infrastructures: a systematic review of modeling techniques, validation and scenario simulation in ENVI-met V4. Build. Environ. 200, 107939. https://doi.org/10.1016/j.buildenv.2021.107939.

Maronga, B., Gross, G., Raasch, S., Banzhaf, S., Forkel, R., Heldens, W., Kanani-Sühring, F., Matzarakis, A., Mauder, M., Pavlik, D., Pfaffenrott, J., Schubert, S., Seckmeyer, G., Sieker, H., Winderlich, K., 2019. Development of a new urban climate model based on the model PALM - Project overview, planned work, and first achievements. Meteorol. Z. 1–15.

Matzarakis, A., Rutz, F., Mayer, H., 2010. Modelling radiation fluxes in simple and complex environments: basics of the RayMan model. Int. J. Biometeorol. 54, 131–139. https://doi.org/10.1007/s00484-009-0261-0.

O'Malley, C., Piroozfar, P., Farr, E.R.P., Pomponi, F., 2015. Urban Heat Island (UHI) mitigating strategies: a case-based comparative analysis. Sustain. Cities Soc. 19, 222–235. https://doi.org/10.1016/j.scs.2015.05.009.

Ouyang, W., Sinsel, T., Simon, H., Morakinyo, T.E., Liu, H., Ng, E., 2022. Evaluating the thermal-radiative performance of ENVI-met model for green infrastructure typologies: experience from a subtropical climate. Build. Environ. 207, 108427. https://doi.org/10.1016/j.buildenv.2021.108427.

Schöneberger, P., Sinsel, T., Ouyang, W., Tan, Z., Bruse, M., Simon, H., 2025. Enhancing urban microclimate simulations: validating ENVI-met's accuracy in modeling multi-directional radiative fluxes and mean radiant temperature in subtropical Hong Kong. Build. Environ. 284, 113475. https://doi.org/10.1016/j.buildenv.2025.113475.

Simon, H., 2016. Modeling Urban Microclimate. Development, Implementation and Evaluation of New and Improved Calculation Methods for the Urban Microclimate Model ENVI-met (Phd Thesis). Johannes Gutenberg-University Mainz.

Sinsel, T., Simon, H., Ouyang, W., dos Santos Gusson, C., Shinzato, P., Bruse, M., 2022. Implementation and evaluation of mean radiant temperature schemes in the microclimate model ENVI-met. Urban Clim. 45, 101279. https://doi.org/10.1016/j.uclim.2022.101279.

Tsoka, S., Tsikaloudaki, A., Theodosiou, T., 2018. Analyzing the ENVI-met microclimate model's performance and assessing cool materials and urban vegetation Applications–A review. Sustain. Cities Soc. 43, 55–76. https://doi.org/10.1016/j.scs.2018.08.009.

Wallenberg, N., Holmer, B., Lindberg, F., Lönn, J., Maesel, E., Rayner, D., 2026. A simple step heating approach for wall surface temperature estimation in the SOlar and LongWave Environmental Irradiance Geometry (SOLWEIG) model. Geosci. Model Dev. 19, 1321–1336. https://doi.org/10.5194/gmd-19-1321-2026.

Wong, N.H., Tan, C.L., Kolokotsa, D.D., Takebayashi, H., 2021. Greenery as a mitigation and adaptation strategy to urban heat. Nat. Rev. Earth Environ. 2, 166–181. https://doi.org/10.1038/s43017-020-00129-5.